RESEARCH ARTICLE-MECHANICAL ENGINEERING

Magnetohydrodynamic Micropolar Nanofluid Flow in a Shrinking Channel with Second-Order Velocity Slip and Thermal Radiation

Nepal Chandra Roy[1] · Ayantika Ghosh[1] · Ioan Pop[2]

Abstract

Magnetohydrodynamic (MHD) micropolar nanofluid flow in a shrinking channel is important due to its use in metallurgical processes, manufacturing industries and industrial applications. In this study, the flow and heat transfer of an electrically conducting micropolar nanofluid passing through a shrinking channel is investigated with the effects of second-order velocity slip conditions and thermal radiation. Using the similarity transformations, the governing dimensional equations were transformed into ordinary differential equations, which have been solved by the finite difference method. The results for skin friction coefficient ($\mathrm{Re}_x^{1/2} C_{\mathrm{fx}}$), couple stress ($m_x$), and local Nusselt number ($\mathrm{Re}_x^{-1/2} \mathrm{Nu}_{\mathrm{fx}}$), as well as flow profiles were presented graphically with variations of material constant (K), volume fraction of alumina nanoparticles (φ), micro-rotation parameter (n), second-order slip parameter (B), first-order slip parameter (A), magnetic parameter (M), suction parameter (S), and radiation parameter (R). The influences of φ, K, n, A, M, and S were significant. With higher K, A, n, and M, $\mathrm{Re}_x^{1/2} C_{\mathrm{fx}}$ and $\mathrm{Re}_x^{-1/2} \mathrm{Nu}_{\mathrm{fx}}$ increased. On the other hand, an increase in S caused a decrease in $\mathrm{Re}_x^{1/2} C_{\mathrm{fx}}$ and an increase in $\mathrm{Re}_x^{-1/2} \mathrm{Nu}_{\mathrm{fx}}$. In the case of higher A and M, velocity increased, but angular velocity decreased. However, the converse was observed for the increase in φ and S. It is worth noting that the boundary layer separation was delayed for increasing values of K, n, A, and M, but accelerated for higher φ, B, and S.

Keywords Micropolar nanofluid · Velocity slip · Magnetohydrodynamic · Shrinking channel · Thermal radiation

List of Symbols

a	Positive constant
A	First-order velocity slip parameter
B	Second-order velocity slip parameter
B_0	Strength of magnetic field (kg s^{-2} A^{-1})
c_p	Heat capacity (J Kg^{-1} K^{-1})
C_{fx}	Skin friction coefficient
h	Distance between bottom and top wall (m)
j	Micro-inertia density
k	Thermal conductivity (W m^{-1} K^{-1})
K	Material parameter
M	Magnetic field parameter
MHD	Magnetohydrodynamic
n	Micro-rotation parameter
$\widehat{N}$	Micro-rotation component
Pr	Prandtl number
S	Suction parameter
$\widehat{T}$	Temperature (K)
T_c	Top wall temperature (K)
T_h	Bottom wall temperature (K)
$\widehat{u}$, $\widehat{v}$	Velocity component (m s^{-1})
u_e	Local edge velocity (m s^{-1})
u_w	Stretched velocity (m s^{-1})
v_w	Mass flux through the wall
v_0	Constant mass flux velocity (m s^{-1})
$\widehat{x}$, $\widehat{y}$	Cartesian coordinates (m)

✉ Nepal Chandra Roy
  nepal@du.ac.bd

[1] Department of Mathematics, University of Dhaka, Dhaka, Bangladesh

[2] Department of Applied Mathematics, Babeş-Bolyai University, Cluj-Napoca, Romania

Greek Symbols

α	Thermal diffusivity (m^2 s^{-1})
β	Coefficient of thermal expansion (K^{-1})
Γ	Micro-inertia parameter

Δ	Surface temperature parameter
θ	Dimensionless temperature
κ	Vortex viscosity
μ	Absolute viscosity (Ns m^{-2})
ν	Kinematic viscosity (m^2 s^{-1})
ρ	Density (kg m^{-3})
σ	Electrical conductivity (A^2 s^3 kg^{-1} m^{-2})
σ_c	Stefan–Boltzmann constant
φ	Volume fraction

Superscript

$(')$	Differentiation with respect to η

Subscripts

f	Base fluid
nf	Nanofluid
s	Nanoparticles

1 Introduction

Micropolar nanofluid flow has been the topic of research because of its various applications in manufacturing industries, aerospace engineering, and metallurgical processes. For industrial purposes, nanofluid flow in a channel is important. Several authors considered micropolar nanofluid flow in different aspects. Saraswathy et al. [1] investigated micropolar fluid flow in a channel with variable surface temperature and variable viscosity. The results were discussed in terms of flow properties considering the variable boundary conditions. Between two parallel plates, Pasha et al. [2] studied the impact of the Peclet number on micropolar fluid flow. They nicely derived the governing equations and compared the consequences with two different numerical methods. Fluid concentration and heat transfer increased with a higher Peclet number. Rehman et al. [3] studied micropolar nanofluid flow in a rectangular geometry. Mahmood et al. [4] explored the peristaltic flow of micropolar fluid in a two-dimensional asymmetric medium taking into account slip conditions. Velocity decreased near the upper wall while increased near the lower wall. Over the surface of a parabola, MHD micropolar fluid flow was examined by Reddy and Reddy [5]. They conducted the study for a three-dimensional case with the effects of thermal radiation. It was reported that the results may be applied to exotic lubricants, polymer fluids, electronic chips, the drawing of copper wire, and artificial fibers.

The combined effects of micro-rotation, Lorentz force, and thermo-migration associated with thermal radiation were analyzed by Xiu et al. [6]. Results showed that the micro-rotation field was strongly dominated by the spins of a tiny number of particles. The spins of the particles were caused by the collision with the boundary. Patel et al. [7] considered the impact of a magnetic field on an unsteady micropolar fluid over a nonlinear stretching sheet. The velocity and temperature profiles were augmented with a larger Eckert number. Sharma and Mishra [8] numerically investigated the time-independent micropolar fluid flow with the thermal radiation effect. The micropolar fluid flow over a stretching sheet with chemical reactions and melting heat transfer was numerically examined by Singh et al. [9]. On the other hand, MHD micropolar fluid flow over a sheet subject to thermal radiation was numerically conducted by Rehman et al. [10].

Due to the lack of heat transfer in the base fluid, nanoparticles are used in the base fluid to enhance thermal conductivity. Fluids with suspended nanomaterials are known as nanofluids. Recent studies [11–13] have experimentally investigated how the nanoparticles affect the thermal conductivity of the nanofluid. Ali et al. [14] examined the enhancement of heat transport by water-based micropolar fluids suspending TiO$_2$ nanoparticles. The finite element scheme was imposed to solve the leading equations. Several studies [15–21] investigated the heat transfer characteristics of nanofluids in different shapes of geometry and boundary conditions.

The stagnation-point micropolar fluid flow along a circular heated object was analyzed by Salahuddin et al. [22]. On the other hand, Abbas et al. [23] illustrated the thermal and velocity slip boundary conditions on MHD micropolar nanofluid flow toward a circular cylinder. They have taken three different types of nanoparticles (Titania, Alumina, and Copper,) and by mixing them with water (the base fluid), they have made three types of nanofluids. From the numerical tables and graphs of the study, it can be observed that copper–water nanofluid showed a strong heat transport rate compared to others. The micropolar fluid flow based on suction or injection, thermal radiation, and gravity modulation was explored by Ali et al. [24]. Outcomes showed that the fluctuation of Nusselt number and temperature increased with higher radiation parameters. Wang et al. [25] reviewed a number of literature on the improvement of heat transfer of nanofluids by applying a magnetic or electric field. They also proposed different effective mechanisms for the improvement of nanofluids. Goud and Nandeppanavar [26] investigated the combined impacts of Ohmic heat and chemical reactions on MHD micropolar fluid along a stretching surface.

Yadav and Kumar [27] studied the entropy production of non-Newtonian micropolar fluid and immiscible Newtonian fluid over a rectangular channel with an inclined magnetic field. They imposed no-slip boundary conditions on the static

wall. A satisfactory derivation of the governing equations was found in the literature. Results were arranged in graphs with variations of physical parameters. Results showed that the friction of the fluid caused by the surface is for the increasing nature of the entropy generation number. It was mentioned that the results could be used in the petroleum industry. Contrary to this, Yusuf et al. [28] examined the entropy generation of micropolar fluid flow with slip effects on a porous medium. Increasing values of micro-rotation parameters increased the entropy generation profiles but declined the velocity profiles. Usafzai and Aly [29] mathematically described the single and multiple exact solutions of a micropolar fluid, considering the constant velocity slip. Kumar et al. [30] explored the effects of velocity slips (first and second order) on micropolar fluid flow in the presence of Lorentz force over a convective surface. It was found that velocity boosted up for second-order slip parameters while temperature was an increasing function of first-order slip parameters.

Su [31] theoretically established a weak solution of compressible micropolar fluid in a bounded domain. On the other hand, Slayi et al. [32] derived the Gauge Uzawa method for incompressible micropolar fluid. Results confirmed the unconditional stability of the method. Some numerical simulations were performed for the validation of theoretical results. The creeping movement of spherical particles in a micropolar fluid orthogonal to the plane interface of a viscous fluid was investigated by Sherief et al. [33]. To examine the comparative outcomes of heat and mass transport of several fluids, Habib et al. [34] analyzed the existence of activation energy, Cattaneo-Christov heat flux, and micro-organism bioconvection over a stretching surface. To compare the results, they have taken four types of fluids: Newtonian fluid, Williamson nanofluid, Maxwell nanofluid, and micropolar nanofluid. The results showed that velocity was higher for micropolar fluid compared to the other fluids.

The above review exposed not only the necessity of in-depth knowledge of MHD micropolar nanofluid flow in a shrinking channel with second-order velocity slip but also its technological importance. However, this topic still remains untouched by the researchers. So, the objective of this study is to investigate electrically conducting micropolar nanofluid flow in a shrinking channel with the effects of second-order velocity slip conditions and thermal radiation. The governing dimensional equations are transformed into a non-dimensional form using a set of similarity variables. These are then solved by the finite difference method. The parametric investigation is carried out in terms of skin friction coefficient, couple stress, local Nusselt numbers, and flow properties. The flowchart of the present work is presented below:
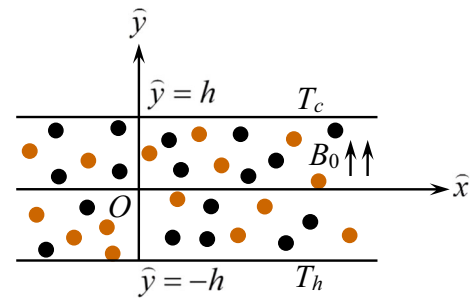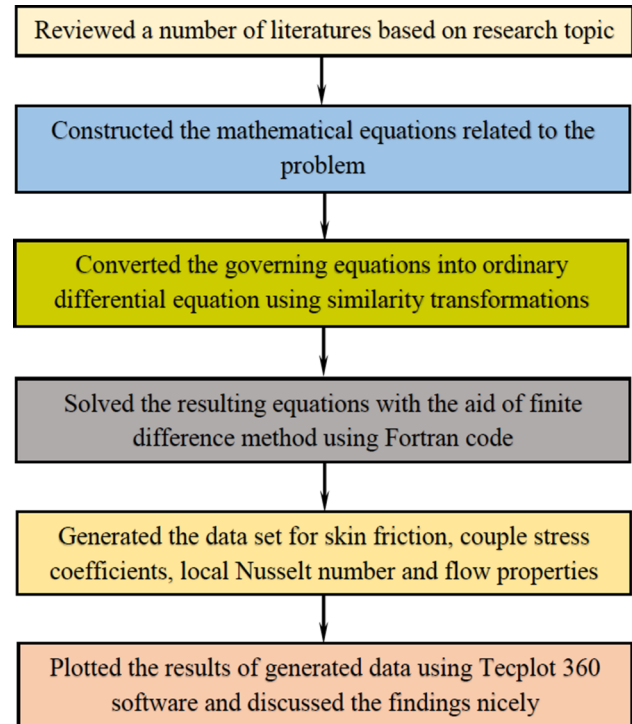

Fig. 1 Schematic of nanofluid flow in a channel

2 Formulation of the Problem

A two-dimensional, steady, micropolar nanofluid flow is considered in a channel with a shrinking wall as presented in Fig. 1, where the Cartesian coordinates are $\left(\widehat{x}, \widehat{y}\right)$, such that the $\widehat{x}$-axis goes along the center of the channel and the $\widehat{y}$-axis is in the orthogonal direction to the channel. A magnetic field of strength B_0 is applied to the fluid along the perpendicular direction of the channel walls. The upper wall's velocity is $\widehat{u} = u_w\left(\widehat{x}\right) = \lambda a\widehat{x}$, where a is a positive constant, $\lambda < 0$ for the shrinking wall and $\lambda = 0$ for a static wall, respectively. Also, T_h, and T_c are the bottom and top wall temperatures, respectively. The walls are located in two horizontal positions $\widehat{y} = \pm h$. As the upper wall is assumed to be shrinking,

velocity slip may happen. However, it is kept at cold temperature and so temperature jump is not considered here. Further assumption between the nanoparticles and the carrier fluid is thermal equilibrium. The fluid is a water (H_2O) based nanofluid containing uniform sized and shaped nanoparticles.

Then, under the usual Boussinesq's approximation, the governing equations for a nanofluid flow in a channel are given as Rees and Pop [35]:

$$\frac{\partial \widehat{u}}{\partial \widehat{x}} + \frac{\partial \widehat{v}}{\partial \widehat{y}} = 0, \tag{1}$$

$$\widehat{u}\frac{\partial \widehat{u}}{\partial \widehat{x}} + \widehat{v}\frac{\partial \widehat{v}}{\partial \widehat{y}} = u_e \frac{\partial u_e}{\partial x} + \frac{\mu_{nf} + \kappa}{\rho_{nf}} \frac{\partial^2 \tilde{u}}{\partial \tilde{y}^2} + \frac{\kappa}{\rho_{nf}} \frac{\partial \widehat{N}}{\partial \widehat{y}}$$
$$- \frac{\sigma_{nf} B_0^2}{\rho_{nf}} \left(\widehat{u} - u_e\right), \tag{2}$$

$$\widehat{u}\frac{\partial \widehat{N}}{\partial \widehat{x}} + \widehat{v}\frac{\partial \widehat{N}}{\partial \widehat{y}} = \frac{1}{\rho_{nf}}\left(\mu_{nf} + \frac{\kappa}{2}\right)\frac{\partial^2 \widehat{N}}{\partial \widehat{y}^2} - \frac{\kappa}{\rho_{nf} j}\left(2\widehat{N} + \frac{\partial \widehat{u}}{\partial \widehat{y}}\right), \tag{3}$$

$$\widehat{u}\frac{\partial \widehat{T}}{\partial \widehat{x}} + \widehat{v}\frac{\partial \widehat{T}}{\partial \widehat{y}} = \alpha_{nf}\frac{\partial^2 \widehat{T}}{\partial \widehat{y}^2} - \frac{1}{(\rho c)_{nf}}\frac{\partial q_{rd}}{\partial \tilde{y}}, \tag{4}$$

with the boundary conditions

$$\widehat{u} = \lambda u_w\left(\widehat{x}\right) + u_{w,\,slip}\left(\widehat{x}\right) = \lambda a\widehat{x} + A_1 \frac{\partial \tilde{u}}{\partial \widehat{y}} + A_2 \frac{\partial^2 \tilde{u}}{\partial \tilde{y}^2},$$

$$N = -n\frac{\partial \tilde{u}}{\partial \widehat{y}}, \ \widehat{T} = T_c \text{ at } \widehat{y} = h,$$

$$\widehat{u} = u_w\left(\widehat{x}\right), \ v = v_w = v_0, \ N = 0, \ \widehat{T} = T_h \text{ at } \widehat{y} = -h, \tag{5}$$

where $\left(\widehat{u}, \ \widehat{v}\right)$ are the components of velocity along $\left(\widehat{x}, \ \widehat{y}\right)$ axes, $u_e\left(\widehat{x}\right) = a\widehat{x}$ is the local edge velocity, $\widehat{T}$ refers the temperature of the nanofluid, $\widehat{N}$ indicates the micro-rotation component orthogonal to the *xy*-plane, v_0 indicates the constant mass flux velocity, where $v_0 > 0$ for suction and $v_0 < 0$ for injection, respectively, κ is the vortex viscosity, j is the microinertia density, (A_1, A_2) are the velocity slip factors, and *n* refers a constant such that $0 \le n \le 1$. In case of *n* = 0, the fluid has a strong concentration, so that the particles near the surface are unable to rotate. For *n* = 1/2, the fluid has a weak concentration, and the particles' spin for fine-particle suspension is same as the fluid vorticity at the surface. However, *n* = 1 corresponds to turbulent boundary

layers. Therefore, an increase in *n* from 0 to 1 relates to the increasing velocity of microelements.

Here the thermophysical properties of the nanofluid are expressed according to Refs. [36, 37]:

$$\rho_{nf} = (1 - \varphi)\rho_f + \varphi\rho_s, \ \mu_{nf}/\mu_f = 1 + 4.93\varphi + 222.4\varphi^2,$$
$$\kappa_{nf}/\kappa_f = 1 + 2.944\varphi + 19.67\varphi^2,$$
$$(\rho c)_{nf}/(\rho c)_f = 1 - \varphi + \varphi(\rho c)_s/(\rho c)_f,$$
$$(\rho c)_{nf}/(\rho c)_f = 1 - \varphi + \varphi(\rho c)_s/(\rho c)_f,$$
$$\sigma_{nf}/\sigma_f = \frac{(\sigma_s/\sigma_f + 2) + 2(\sigma_s/\sigma_f - 1)\varphi}{(\sigma_s/\sigma_f + 2) - (\sigma_s/\sigma_f - 1)\varphi}. \tag{6}$$

In Eq. (6), (ρ_f, ρ_s) are densities, (μ_{nf}, μ_f) are dynamic viscosities, $((\rho c)_f, (\rho c)_s)$ are heat capacities, and, (σ_f, σ_s) are electrical conductivities of the conventional fluid and nanoparticles, respectively, α_f is the thermal diffusivity of the fluid, and φ is the nanoparticles volume fraction. The subscript nf represents the quantities of the nanofluid. It is mentioned that $\varphi = 0$ indicates a regular fluid. In Table 1, the characteristics of the base fluid and nanoparticles are tabulated.

In this study, the radiative heat flux q_{rd} is defined below based on Rosseland approximation [39–41]:

$$q_{rd} = -\frac{4\sigma_c}{3k_c}\frac{\partial \widehat{T}^4}{\partial \widehat{y}}, \tag{7}$$

where k_c denotes the mean absorption coefficient, and σ_c stands for the Stefan-Boltzmann constant.

Guided by the boundary condition (5), the similarity variables are defined as,

$$\widehat{u} = a\widehat{x}f'(\eta), \ \widehat{v} = -\left(av_f\right)^{1/2}f(\eta), \ N = a(a/v_f)^{1/2}\widehat{x}g(\eta),$$
$$\theta(\eta) = \frac{T - T_c}{T_h - T_c}, \ \eta = \left(a/v_f\right)^{1/2}\widehat{y}. \tag{8}$$

Table 1 Thermo-physical characteristics of H_2O and Al_2O_3 nanoparticles [38]

Physical characteristics	Fluid (H_2O)	Al_2O_3
c_p (Jkg^{-1} K^{-1})	4179	765
ρ (kgm^{-3})	997.1	3970
κ (Wm^{-1} K^{-1})	0.613	40
$\beta \times 10^{-5}$ (K^{-1})	21	0.85
σ ($\Omega/m)^{-1}$	0.05	3.69×10^7

Table 2 Values of $-f''(0)$ and $-\theta'(0)$

K	S	G	$-f''(0)$		$-\theta'(0)$	
			Ref. [43]	Present	Ref. [43]	Present
0.2	-0.5	2	0.3561	0.35871	0.3776	0.38607
0.1	-0.5	2	0.3636	0.36509	0.3769	0.38580
0.1	-0.5	4	0.3660	0.36662	0.3767	0.38583
0.1	-0.7	2	0.2850	0.28500	0.1348	0.13877

Table 3 Values of $f''(0)$ and $g'(0)$

K	S	n	$f''(0)$		$g'(0)$	
			Ref. [44]	Present	Ref. [44]	Present
0.1	-0.5	0.0	0.1150	0.11613	-0.0313	-0.03011
0.1	-0.5	0.5	0.1175	0.11844	0.0003	0.00071
0.1	-0.5	1.0	0.1201	0.12084	0.0330	0.03278
0.1	1.0	0.5	0.1966	0.19761	-0.0169	-0.01665

so that

$$v_{\mathrm{w}} = v_0 = -(a v_{\mathrm{f}})^{1/2} S, \qquad (9)$$

where primes denotes differentiation with respect to η and S indicate the constant mass flux velocity, where $S > 0$ indicates suction and $S < 0$ indicates injection, respectively.

$$\left(\frac{\mu_r + K}{\rho_r}\right) f''' + f f'' + 1 - f'^2 + \frac{K}{\rho_r} g' - M \frac{\sigma_r}{\rho_r} \left(f' - 1\right) = 0, \qquad (10)$$

$$\left(\frac{\mu_r + K}{2\rho_r}\right) g'' + f g' - f' g - \frac{K}{\rho_r} \Gamma \left(2g + f''\right) = 0, \qquad (11)$$

$$\frac{1}{\mathrm{Pr}} \left\{ \alpha_r + \frac{4R}{3(\rho c)_r} (1 + \Delta\theta)^3 \right\} \theta''$$
$$+ \frac{4\Delta}{\mathrm{Pr}(\rho c)_r} (1 + \Delta\theta)^2 \theta'^2 + f\theta' = 0. \qquad (12)$$

where $\rho_r = \rho_{\mathrm{nf}}/\rho_{\mathrm{f}}$, $\mu_r = \mu_{\mathrm{nf}}/\mu_{\mathrm{f}}$, $\alpha_r = \alpha_{\mathrm{nf}}/\alpha_{\mathrm{f}}$, $(\rho C)_r = (\rho C)_{\mathrm{nf}}/(\rho C)_{\mathrm{f}}$, α_{f} is known as thermal diffusivity of the fluid, $\mathrm{Pr} = v_{\mathrm{f}}/\alpha_{\mathrm{f}}$ is the Prandtl number, $R = 4\sigma_c T_c^3/(k_c \kappa_{\mathrm{f}})$ stands for the radiation parameter, $K = \kappa/\mu_{\mathrm{f}}$ indicates the material parameter, $M = \sigma_f B_0^2/(\rho_f a)$ refers the magnetic parameter, $\Gamma = v_{\mathrm{f}}/(ja)$ is the microinertia parameter, and $\Delta = T_h/T_c - 1$ is the surface temperature parameter.

The boundary conditions are

$$f = 0, \quad f' = \lambda + A f'' + B f''',$$
$$g = -n f'', \quad \theta = 0 \text{ at } \eta = 1, \qquad (13)$$
$$f = S, \quad f' = 1, \quad g = 0, \quad \theta = 1 \text{ at } \eta = -1.$$

here A and B are the first- and second-order velocity slip parameters with $0 < A < (a/v_f)^{1/2}$ and $-a/v_f < B < 0$.

Now the results are analyzed in terms of local skin friction coefficient, C_{fx}, couple stress coefficient, m_x, and local Nusselt number, Nu_x, as defined below:

$$C_{fx} = \frac{1}{\rho_{\mathrm{nf}} u_w^2} \left[(\mu_{\mathrm{nf}} + \kappa) \left(\frac{\partial \widehat{u}}{\partial \widehat{y}}\right)_{\widehat{y}=-h} + \kappa \widehat{N} \right],$$

$$m_x = \frac{x}{\rho_{\mathrm{nf}} u_w^2} \left(\mu_{\mathrm{nf}} + \frac{\kappa}{2}\right) \left(\frac{\partial \widehat{N}}{\partial \widehat{y}}\right)_{\widehat{y}=-h},$$

$$\mathrm{Nu}_x = -\frac{\widehat{x}}{\kappa_{\mathrm{f}}(T_h - T_c)} \left[\kappa_{\mathrm{nf}} \left(-\frac{\partial \widetilde{T}}{\partial \widetilde{y}}\right)_{\widehat{y}=-h} + (q_{\mathrm{rd}})_{\widehat{y}=-h} \right] \qquad (14)$$

Using the definitions of (5) into (23), we find

$$\mathrm{Re}_x^{1/2} C_{fx} = \frac{\rho_{\mathrm{f}}}{\rho_{\mathrm{nf}}} \left\{ \frac{\mu_{\mathrm{nf}}}{\mu_{\mathrm{f}}} + (1 - n) K \right\} f''(-1),$$

$$m_x = \frac{\rho_{\mathrm{f}}}{\rho_{\mathrm{nf}}} \left(\frac{\mu_{\mathrm{nf}}}{\mu_{\mathrm{f}}} + \frac{K}{2}\right) g'(-1), \qquad (15)$$

and $\mathrm{Re}_x^{-1/2} \mathrm{Nu}_x = -\left(\frac{\kappa_{\mathrm{nf}}}{\kappa_{\mathrm{f}}} + \frac{4}{3} R (1 + \Delta\theta)^3\right) \theta'(-1),$

where $\mathrm{Re}_x = u_w \widehat{x}/v_{\mathrm{f}}$ stands for local Reynolds number.
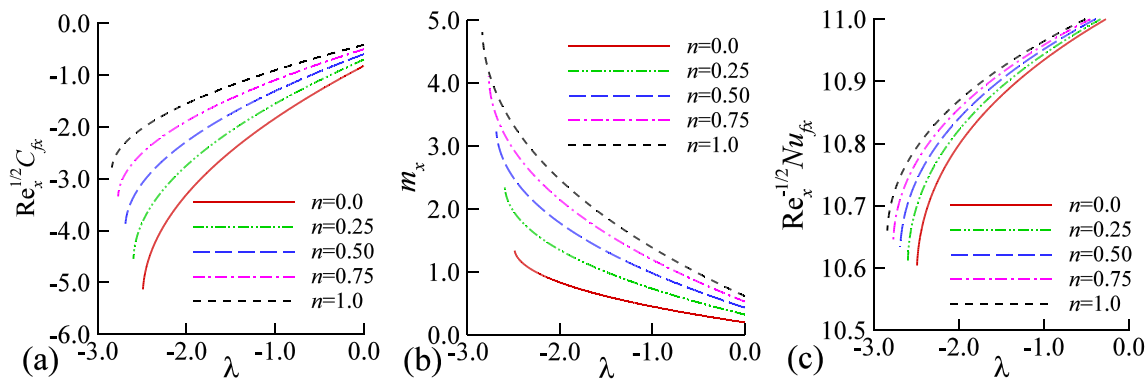
Fig. 2 Variations in **a** $\mathrm{Re}_x^{1/2}C_{\mathrm{fx}}$, **b** m_x, and **c** $\mathrm{Re}_x^{-1/2}\mathrm{Nu}_{\mathrm{fx}}$ for different n, when $\varphi = 0.05$, $S = 2.5$, $K = 1.0$, $B = 2.0$, $A = 2.0$, $M = 1.0$, and $R = 1.0$
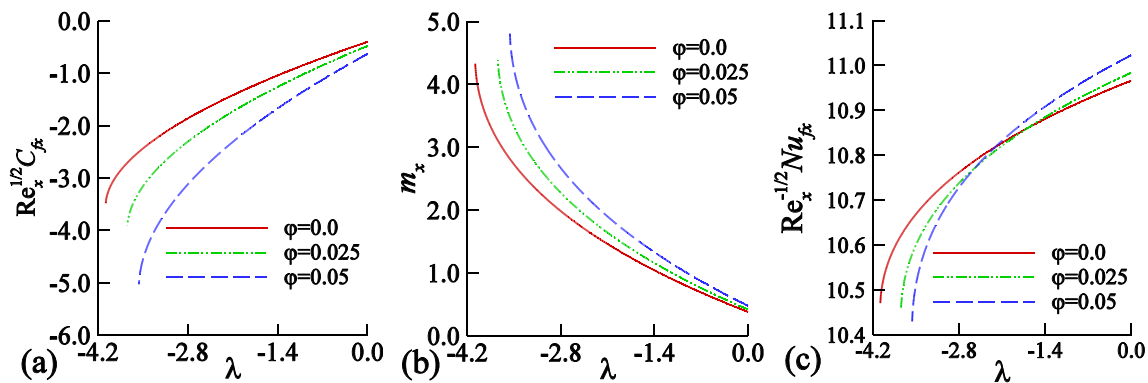
Fig. 3 Variations in **a** $\mathrm{Re}_x^{1/2}C_{\mathrm{fx}}$, **b** m_x, and **c** $\mathrm{Re}_x^{-1/2}\mathrm{Nu}_{\mathrm{fx}}$ for different φ, when $n = 0.5$, $S = 2.5$, $K = 1.0$, $B = 2.0$, $A = 2.0$, $M = 1.0$, and $R = 1.0$
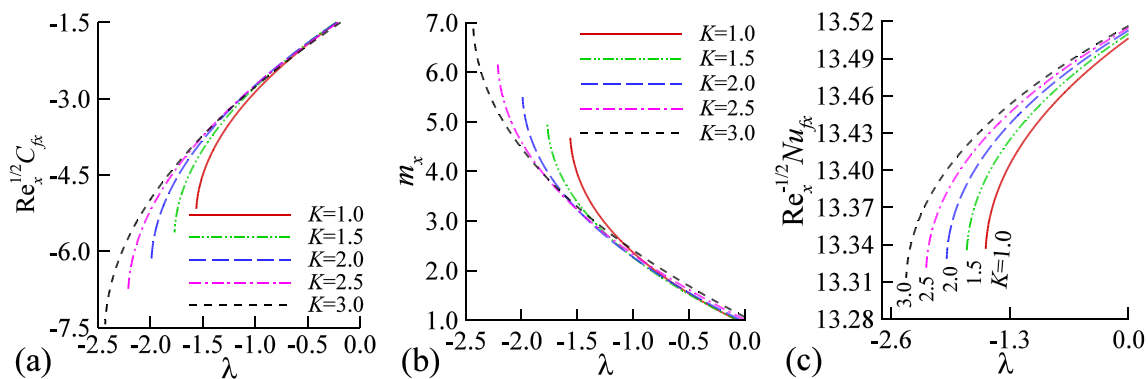
Fig. 4 Variations in **a** $\mathrm{Re}_x^{1/2}C_{\mathrm{fx}}$, **b** m_x, and **c** $\mathrm{Re}_x^{-1/2}\mathrm{Nu}_{\mathrm{fx}}$ for higher K, when $\varphi = 0.05$, $S = 3.0$, $n = 0.5$, $A = 1.0$, $B = 1.0$, $M = 0.5$, and $R = 0.5$

3 Results and discussion

In this study, Eqs. (10–12) with boundary conditions (13) are solved using the finite difference method. To implement this method, Eq. (10) is first reduced to a second-order differential equation taking $V = f$ and $U = f'$:

$$\left(\frac{\mu_r + K}{\rho_r}\right) U'' + V U' + 1 - U^2 + \frac{K}{\rho_r} g' - M \frac{\sigma_r}{\rho_r}(U - 1) = 0.$$

$$(16)$$

Now the Eqs. (11), (12) and (16) are discretized employing the central difference formula. The resulting equations are tridiagonal algebraic equations of the form:

$$B_n \Gamma_{i-1} + A_n \Gamma_i + C_n \Gamma_{i+1} = R_{n,i}.$$

$$(17)$$

In the above equation, the subscript $i \, (= 1, 2, \ldots, M_\eta)$ is the grid point in η direction, $M_\eta = 2001$ is the total number of grids, $n = 1, 2, 3$ corresponds to U, g and θ, respectively. For a fixed n, the tridiagonal system (17) is solved utilizing Thomas algorithm [42]. The convergence criterion for the
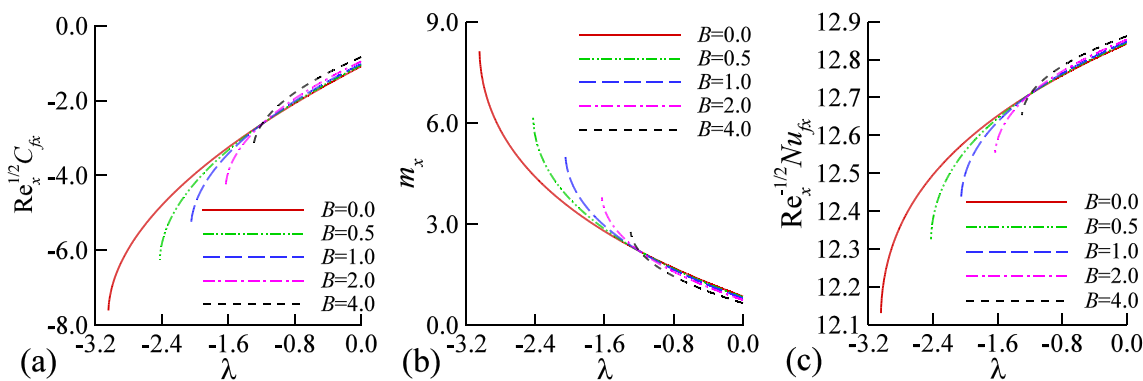
Fig. 5 Variations in **a** $\mathrm{Re}_x^{1/2}C_{\mathrm{fx}}$, **b** m_x, and **c** $\mathrm{Re}_x^{-1/2}\mathrm{Nu}_{\mathrm{fx}}$ for higher B, when $\varphi = 0.05$, $S = 3.0$, $K = 1.0$, $A = 1.0$, $n = 0.5$, $M = 1.0$, and $R = 1.0$
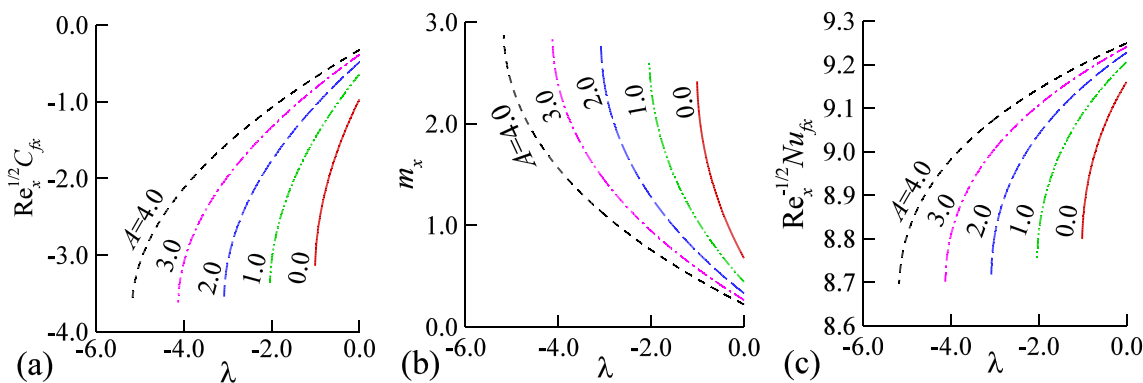
Fig. 6 Variations in **a** $\mathrm{Re}_x^{1/2}C_{fx}$, **b** m_x, and **c** $\mathrm{Re}_x^{-1/2}\mathrm{Nu}_{fx}$ for higher A, when $\varphi = 0.05$, $S = 2.0$, $n = 0.5$, $K = 1.0$, $B = 2.0$, $M = 1.0$, and $R = 1.0$
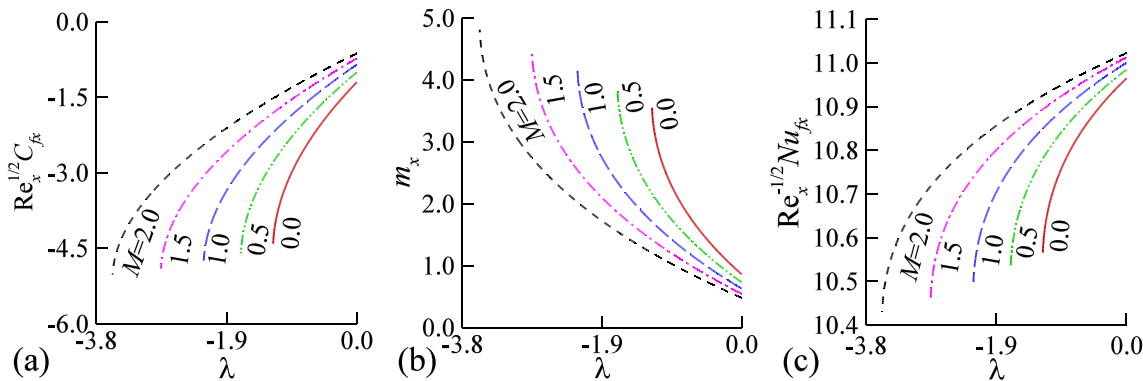
Fig. 7 Variations in **a** $\mathrm{Re}_x^{1/2}C_{\mathrm{fx}}$, **b** m_x, and **c** $\mathrm{Re}_x^{-1/2}\mathrm{Nu}_{\mathrm{fx}}$ for higher M, when $\varphi = 0.05$, $S = 2.5$, $n = 0.5$, $K = 1.0$, $B = 1.0$, $A = 1.0$, and $R = 1.0$

numerical solutions is less than 10^{-5}. Once U is found, f can easily be determined from the relation $U = f'$.

Before discussing the results, a comparison is presented to validate the present numerical solutions. When $n = 0.0$, $\lambda = 0.0$, $M = 0.0$, $A = 0.0$, $B = 0.0$, $R = 0.0$, $\Delta = 0.0$, $\varphi = 0.0$, third and fourth terms of Eq. (10) are zero, second and third terms of Eq. (11) are zero, the coefficient of f''' is unity, coefficient of g'' is G, domain of solutions $[-1, 1]$ is $[0, \eta_{\max}]$, and the boundary condition $f'(0) = 0$, the present problem becomes similar to Takhar and Soundalgekar [43]. Table 2 shows the comparisons between the present results

and corresponding values of Takhar and Soundalgekar [43] which give a good agreement. Moreover, the present model can be considered as in Jena and Mathur [44] by adding and deleting some terms in Eqs. (10–12). A comparison is shown in Table 3 which provides an excellent agreement.

The influences of micro-rotation parameter, n, on $\mathrm{Re}_x^{1/2}C_{\mathrm{fx}}$, m_x, and $\mathrm{Re}_x^{-1/2}\mathrm{Nu}_{\mathrm{fx}}$ are elucidated in Fig. 2a–c. For a fixed n, when λ is slowly decreased, then $\mathrm{Re}_x^{1/2}C_{\mathrm{fx}}$ and $\mathrm{Re}_x^{-1/2}\mathrm{Nu}_{\mathrm{fx}}$ monotonically decrease and m_x increases. With further decrease in λ, these quantities tend to their asymptotic values at a certain value of λ which is known
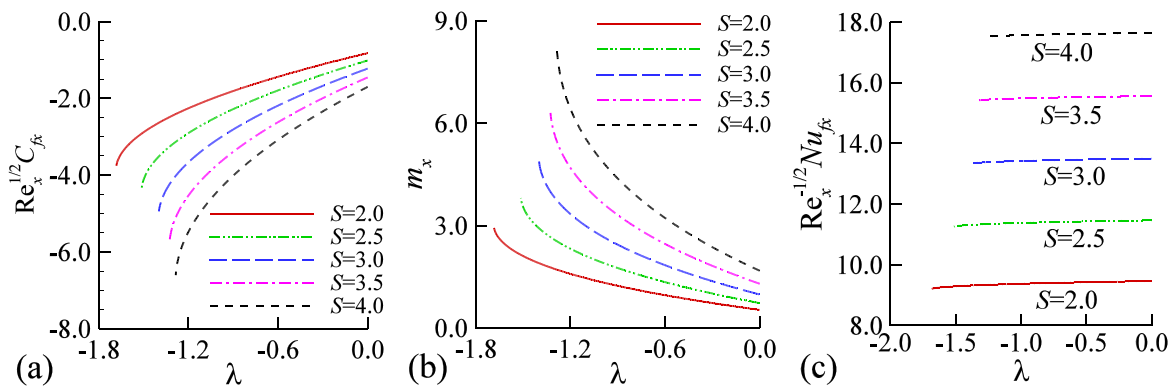
Fig. 8 Variations in **a** $\mathrm{Re}_x^{1/2}C_{\mathrm{fx}}$, **b** m_x, and **c** $\mathrm{Re}_x^{-1/2}\mathrm{Nu}_{\mathrm{fx}}$ for higher S, when $\varphi = 0.05$, $n = 0.5$, $M = 0.5$, $K = 0.5$, $B = 1.0$, $A = 1.0$, and $R = 0.5$
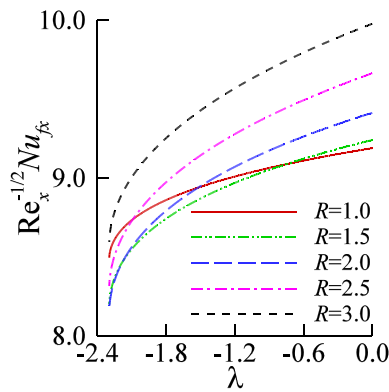

Fig. 9 Variations in $\mathrm{Re}_x^{-1/2}\mathrm{Nu}_{\mathrm{fx}}$ for higher R, when $\varphi = 0.05$, $M = 0.5$, $n = 0.5$, $K = 2.0$, $B = 1.0$, $A = 1.0$, and $S = 2.0$

as critical point of λ and denoted by λ_c. For $n = 0.0, 0.25, 0.50, 0.75$, and 1.0 the critical points of (λ_c, $\mathrm{Re}_x^{1/2}C_{\mathrm{fx}}$, m_x, $\mathrm{Re}_x^{-1/2}\mathrm{Nu}_{\mathrm{fx}}$) are ($-2.49000$, -5.13309, 10.60400, 1.33849), (-2.59750, -4.54428, 10.61009, 2.36997), (-2.68750, -3.86584, 10.63340, 3.23197), (-2.77000, -3.34062, 10.64091, 4.11338), and (-2.84000, -2.78209, 10.66011, 4.81145). It suggests that higher n augments $|\lambda_c|$ and delays the boundary layer separation. Results show the noticeable enhancement in $\mathrm{Re}_x^{1/2}C_{\mathrm{fx}}$ and m_x with higher n. The curves also show that the highest values of $\mathrm{Re}_x^{1/2}C_{\mathrm{fx}}$, m_x, and $\mathrm{Re}_x^{-1/2}\mathrm{Nu}_{\mathrm{fx}}$ are found at $n = 1.0$. For $n = 1.0$, the concentration of the fluid is lower, which leads to the increase in fluid velocity. Also, $\mathrm{Re}_x^{-1/2}\mathrm{Nu}_{\mathrm{fx}}$ increases with higher n, but the increasing rate is slower than $\mathrm{Re}_x^{1/2}C_{\mathrm{fx}}$, and m_x.

In Fig. 3a–c, the effects of φ on $\mathrm{Re}_x^{1/2}C_{\mathrm{fx}}$, m_x, and $\mathrm{Re}_x^{-1/2}\mathrm{Nu}_{\mathrm{fx}}$ are depicted. Due to the increase in φ, the value of $\mathrm{Re}_x^{1/2}C_{\mathrm{fx}}$ is noticeably decreased and m_x is increased. However, when φ is increased, the value of $\mathrm{Re}_x^{-1/2}\mathrm{Nu}_{\mathrm{fx}}$ is higher for $\lambda \geq -2.2$ and lower for $\lambda < -2.2$. It can be understood from the fact that the inclusion of heavier nanoparticles reduce the fluid velocity. Moreover, the stronger shrinking velocity diminishes the heat transfer from the surface to the fluid. For $\varphi = 0.0, 0.025, 0.05$,

the critical points of (λ_c, $\mathrm{Re}_x^{1/2}C_{\mathrm{fx}}$, m_x, $\mathrm{Re}_x^{-1/2}\mathrm{Nu}_{\mathrm{fx}}$) are ($-4.08000$, -3.47943, 10.47069, 4.33102), (-3.74250, -3.90046, 10.46082, 4.38944), (-3.56250, -5.02539, 10.43017, 4.81063). Therefore, the higher φ reduces $|\lambda_c|$ and so it accelerates the boundary layer separation.

Figure 4a–c describe the effects of material constant, K, on $\mathrm{Re}_x^{1/2}C_{\mathrm{fx}}$, m_x, and $\mathrm{Re}_x^{-1/2}\mathrm{Nu}_{\mathrm{fx}}$. For higher values of K, $\mathrm{Re}_x^{1/2}C_{\mathrm{fx}}$ and $\mathrm{Re}_x^{-1/2}\mathrm{Nu}_{\mathrm{fx}}$ are higher. However, m_x shows a distinct behavior depending on the value of λ. When K increases, a significant increase in $\mathrm{Re}_x^{-1/2}\mathrm{Nu}_{\mathrm{fx}}$ is found. For $K = 1.0, 1.5, 2.0, 2.5$, and 3.0, the values of (λ_c, $\mathrm{Re}_x^{1/2}C_{\mathrm{fx}}$, m_x, $\mathrm{Re}_x^{-1/2}\mathrm{Nu}_{\mathrm{fx}}$) are ($-1.56250$, -5.16558, 13.33656, 4.67991), (-1.77000, -5.62940, 13.33346, 4.99653), (-1.77000, -5.62940, 13.33346, 4.99653), (-2.21250, -6.77470, 13.32125, 6.15376), and (-2.43250, -7.43634, 13.31315, 6.90201). In this regard, increasing K augments the domain (λ_c, 0) of boundary layer approximation.

Figures 5a–c exhibit the impacts of second-order slip parameter, B, on $\mathrm{Re}_x^{1/2}C_{\mathrm{fx}}$, m_x, and $\mathrm{Re}_x^{-1/2}\mathrm{Nu}_{\mathrm{fx}}$. Due to the increasing values of B, $\mathrm{Re}_x^{1/2}C_{\mathrm{fx}}$ and $\mathrm{Re}_x^{-1/2}\mathrm{Nu}_{\mathrm{fx}}$ are higher near $\lambda = 0.0$ then become lower for decreasing λ. The converse is found for variations in m_x. This is because the second-order velocity slip parameter slows down the fluid velocity. For $B = 0.0, 0.5, 1.0, 2.0$, and 4.0 the values of (λ_c, $\mathrm{Re}_x^{1/2}C_{\mathrm{fx}}$, m_x, $\mathrm{Re}_x^{-1/2}\mathrm{Nu}_{\mathrm{fx}}$) are ($-3.04500$, -7.60761, 12.13064, 8.13728), (-2.42500, -6.24009, 12.32572, 6.16187), (-2.05000, -5.30791, 12.43843, 4.99621), (-1.63000, -4.23681, 12.55424, 3.79354), and (-1.29750, -3.22834, 12.65335, 2.76880). It indicates that higher B reduces $|\lambda_c|$ and hence accelerates the boundary layer separation.

In Fig. 6a–c the effects of first-order slip parameter, A, on $\mathrm{Re}_x^{1/2}C_{\mathrm{fx}}$, m_x, and $\mathrm{Re}_x^{-1/2}\mathrm{Nu}_{\mathrm{fx}}$ are illustrated. Results reveal that $\mathrm{Re}_x^{1/2}C_{\mathrm{fx}}$ and $\mathrm{Re}_x^{-1/2}\mathrm{Nu}_{\mathrm{fx}}$ are higher and m_x is lower with the increase in A. For $A = 0.0, 1.0, 2.0, 3.0$, and 4.0, the critical values of (λ_c, $\mathrm{Re}_x^{1/2}C_{\mathrm{fx}}$, m_x, $\mathrm{Re}_x^{-1/2}\mathrm{Nu}_{\mathrm{fx}}$) are ($-1.01000$, -3.14097, 8.79938, 2.41515), (-2.03750, -3.36592, 8.75435, 2.61731), (-3.08000,
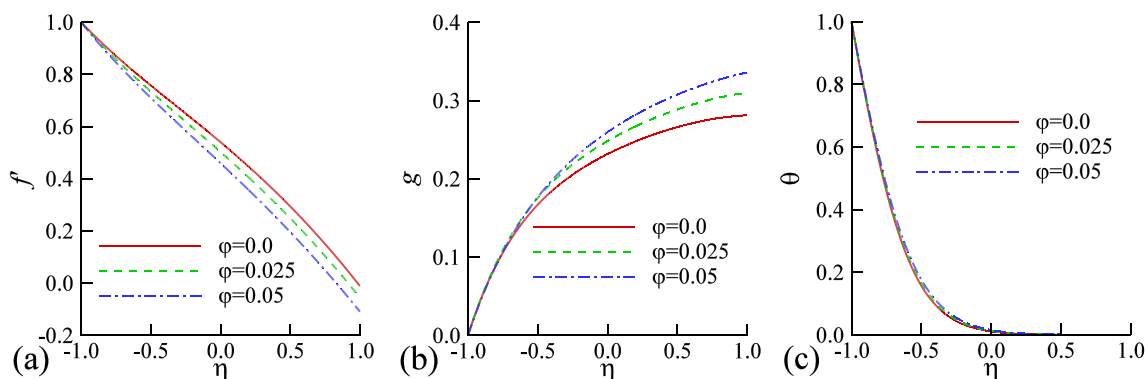
Fig. 10 Variations in **a** f', **b** g, and **c** θ for changing φ, when $K = 1.0$, $S = 3.0$, $n = 0.5$, $A = 1.0$, $B = 1.0$, $M = 0.5$, $R = 0.5$, and $\lambda = -1.0$

Fig. 11 Variations in **a** f' and **b** g for changing K, when $\varphi = 0.05$, $S = 3.0$, $n = 0.5$, $A = 1.0$, $B = 1.0$, $M = 0.5$, $R = 0.5$, and $\lambda = -1.0$
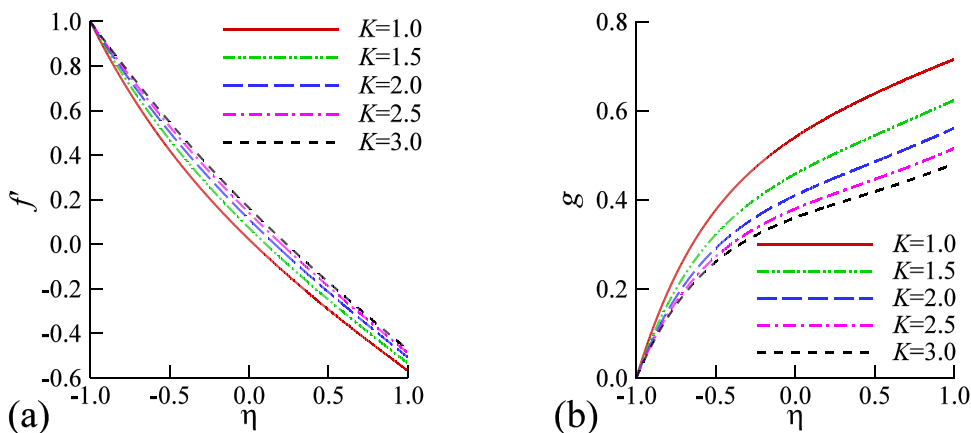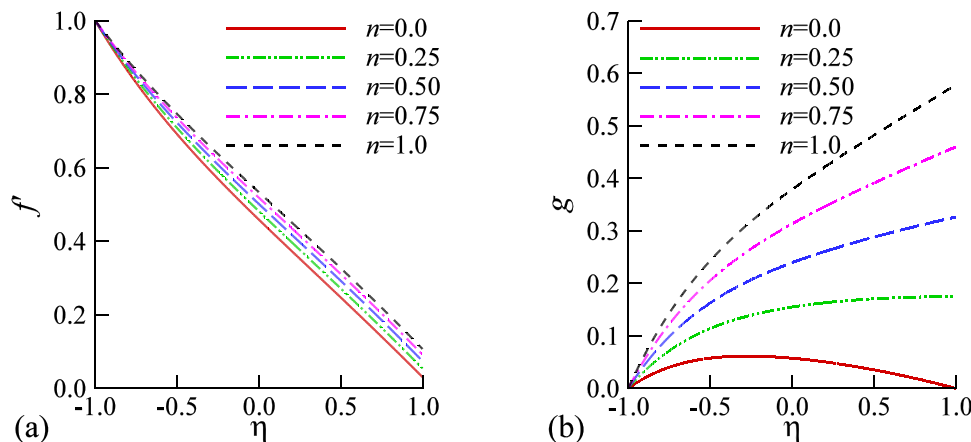

Fig. 12 Variations in **a** f' and **b** g for higher n, when $\varphi = 0.05$, $S = 2.5$, $K = 1.0$, $A = 2.0$, $M = 1.0$, $B = 2.0$, $R = 1.0$, and $\lambda = -1.0$

-3.54222, 8.71767, 2.77925), $(-4.12750, -3.61950, 8.70118, 2.85124)$, and $(-5.17750, -3.64656, 8.69534, 2.87660)$. These results imply that $|\lambda_c|$ increases with A and so the boundary layer separation becomes delay for increasing A.

The influences of magnetic parameter, M, on $\text{Re}_x^{1/2}C_{\text{fx}}$, m_x, and $\text{Re}_x^{-1/2}\text{Nu}_{\text{fx}}$ are exhibited in Fig. 7a–c. One can easily observe that an increase in M reduces m_x but augments $\text{Re}_x^{1/2}C_{\text{fx}}$ and $\text{Re}_x^{-1/2}\text{Nu}_{\text{fx}}$. It is because the magnetic field impedes the flow velocity. For $M = 0.0, 0.5, 1.0, 1.5$, and

2.0, the critical points of (λ_c, $\text{Re}_x^{1/2}C_{\text{fx}}$, m_x, $\text{Re}_x^{-1/2}\text{Nu}_{\text{fx}}$) are $(-1.22000, -4.40988, 10.56570, 3.55113)$, $(-1.69000, -4.59059, 10.53128, 3.84671)$, $(-2.23250, -4.74686, 10.49830, 4.14691)$, $(-2.85500, -4.90565, 10.46225, 4.48337)$, and $(-3.56250, -5.02539, 10.43017, 4.81063)$. Since the value of $|\lambda_c|$ increases with the increase in M, hence the boundary layer approximation is valid for larger shrinking velocity.

Figure 8a–c depicts the impacts of suction parameter, S, on $\text{Re}_x^{1/2}C_{\text{fx}}$, m_x, and $\text{Re}_x^{-1/2}\text{Nu}_{\text{fx}}$. For $S = 4.0$, $\text{Re}_x^{1/2}C_{\text{fx}}$

Fig. 13 Variations in **a** f' and **b** g for higher B, when $\varphi = 0.05$, $S = 3.0$, $K = 1.0$, $A = 1.0$, $n = 0.5$, $M = 1.0$, $R = 1.0$, and $\lambda = -1.0$
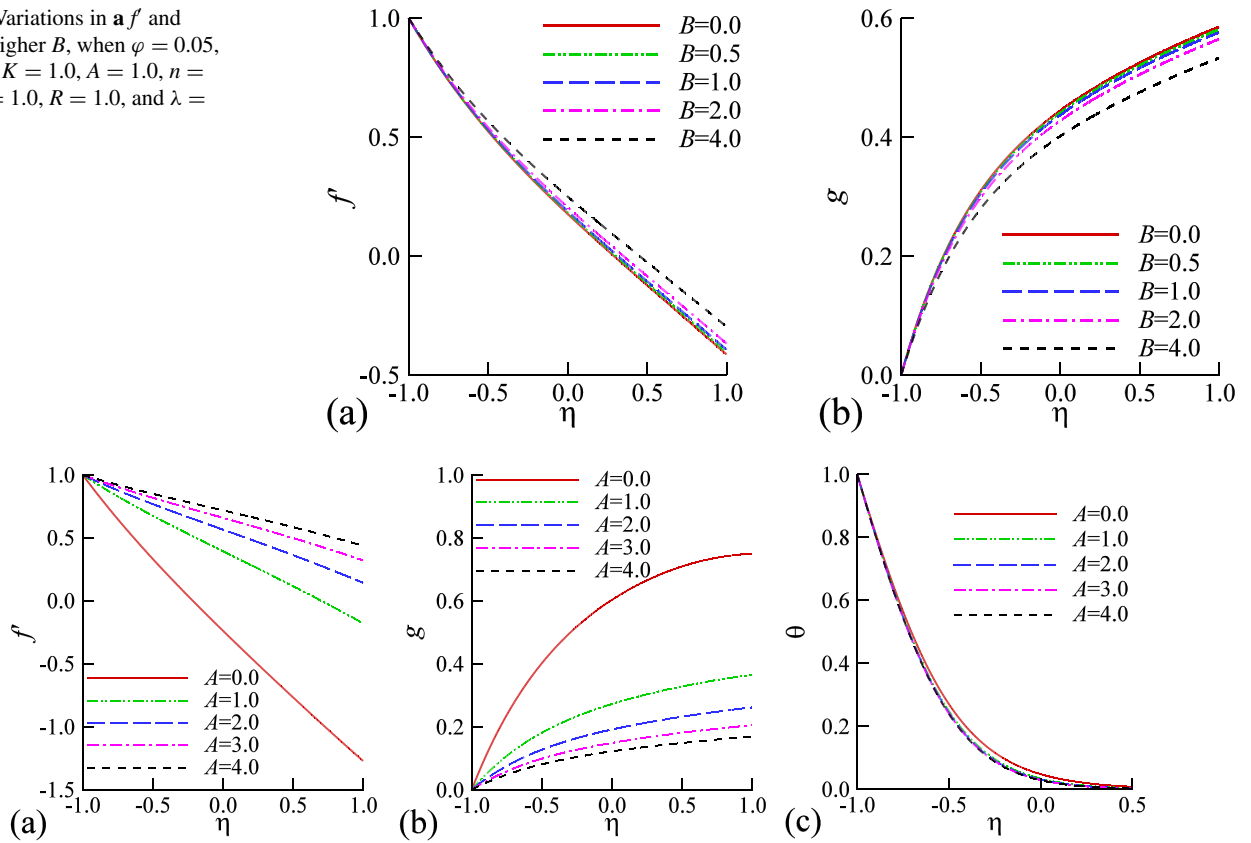

Fig. 14 Variations in **a** f', **b** g, and **c** θ for higher A, when $\varphi = 0.05$, $S = 2.0$, $n = 0.5$, $K = 1.0$, $B = 2.0$, $M = 1.0$, $R = 1.0$, and $\lambda = -1.0$
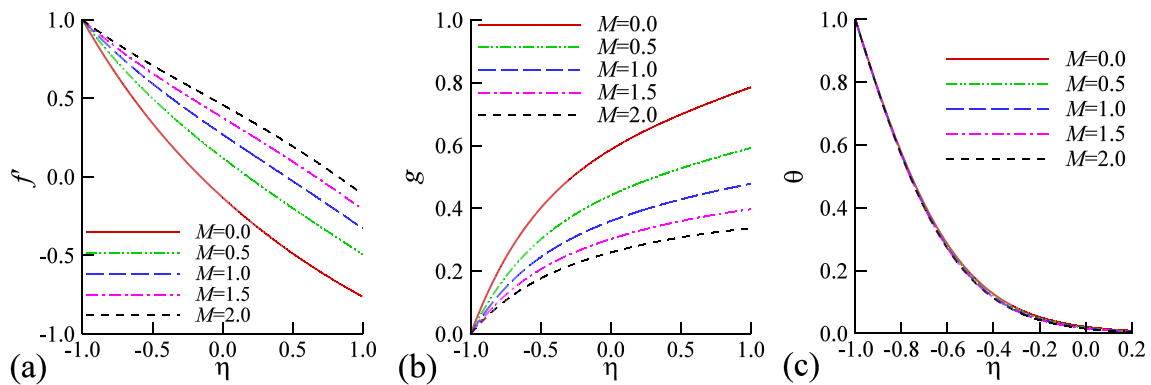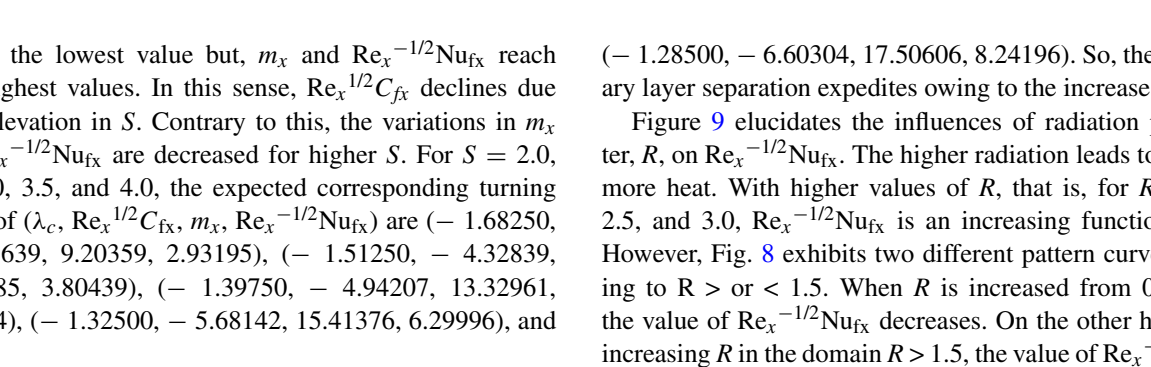

Fig. 15 Variations in **a** f', **b** g, and **c** θ for higher M, when $\varphi = 0.05$, $S = 2.5$, $n = 0.5$, $K = 1.0$, $B = 1.0$, $A = 1.0$, $R = 1.0$, and $\lambda = -1.0$

obtains the lowest value but, m_x and $\mathrm{Re}_x^{-1/2}\mathrm{Nu}_{\mathrm{fx}}$ reach their highest values. In this sense, $\mathrm{Re}_x^{1/2}C_{\mathrm{fx}}$ declines due to an elevation in S. Contrary to this, the variations in m_x and $\mathrm{Re}_x^{-1/2}\mathrm{Nu}_{\mathrm{fx}}$ are decreased for higher S. For $S = 2.0$, 2.5, 3.0, 3.5, and 4.0, the expected corresponding turning points of $(\lambda_c, \mathrm{Re}_x^{1/2}C_{\mathrm{fx}}, m_x, \mathrm{Re}_x^{-1/2}\mathrm{Nu}_{\mathrm{fx}})$ are $(-1.68250, -3.75639, 9.20359, 2.93195)$, $(-1.51250, -4.32839, 11.25685, 3.80439)$, $(-1.39750, -4.94207, 13.32961, 4.87724)$, $(-1.32500, -5.68142, 15.41376, 6.29996)$, and

$(-1.28500, -6.60304, 17.50606, 8.24196)$. So, the boundary layer separation expedites owing to the increase in S.

Figure 9 elucidates the influences of radiation parameter, R, on $\mathrm{Re}_x^{-1/2}\mathrm{Nu}_{\mathrm{fx}}$. The higher radiation leads to radiate more heat. With higher values of R, that is, for $R = 2.0$, 2.5, and 3.0, $\mathrm{Re}_x^{-1/2}\mathrm{Nu}_{\mathrm{fx}}$ is an increasing function of R. However, Fig. 8 exhibits two different pattern curves relating to R > or < 1.5. When R is increased from 0 to 1.5, the value of $\mathrm{Re}_x^{-1/2}\mathrm{Nu}_{\mathrm{fx}}$ decreases. On the other hand, for increasing R in the domain R > 1.5, the value of $\mathrm{Re}_x^{-1/2}\mathrm{Nu}_{\mathrm{fx}}$
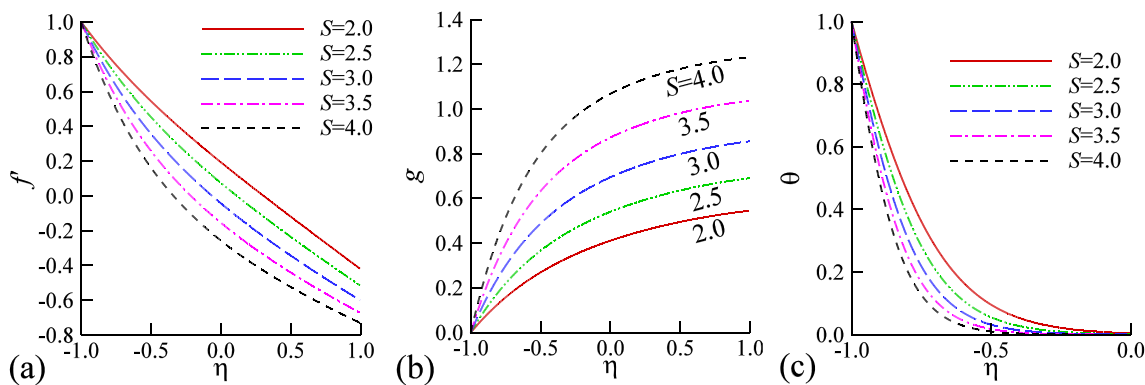
Fig. 16 Variations in **a** f', **b** g and **c** θ for higher S, when $\varphi = 0.05$, $M = 0.5$, $n = 0.5$, $K = 0.5$, $B = 1.0$, $A = 1.0$, $R = 0.5$, and $\lambda = -1.0$

increases. For $R = 1.0$, 1.5, 2.0, 2.5, and 3.0, the values of $(\lambda_c, \mathrm{Re}_x^{-1/2}\mathrm{Nu}_{fx})$ are $(-2.29750, 4.30461)$, $(-2.29750, 4.30461)$, $(-2.29750, 4.30461)$, $(-2.29750, 4.30461)$, and $(-2.29750, 4.30461)$. These indicate that the boundary layer approximation remains unchanged against λ.

The effect of alumina nanoparticles, φ, on f', g, and θ is shown in Fig. 10a–c. An increase in φ causes to decrease in f' and increase in g and θ. It is also evident from Fig. 10a, b that the strong influence of φ is on f' and g. As the fluid becomes heavier with the inclusion of nanoparticles, the fluid velocity is lower for increasing φ. On the contrary, the nanoparticles' thermal conductivity is higher than the pure fluid, resulting in an increase in temperature.

Figure 11a–b illustrates the influences of material constant, K, on f' and g. With larger K, f' grows slowly, but, the converse is found in g. However, the rate of change of f' and g becomes slow for increasing K. The cause is that the material constant K is strongly related to the angular velocity of the fluid, which decreases with higher K. When fluid particles move with lower spin, the fluid velocity is thus accelerated.

The effects of micro-rotation parameter, n, on f' and g are discussed in Fig. 12a–b. Figure 12a shows the slow increase in f', but a rapid increase in g for varying n from lower to higher values. From the definition of n, when $n = 0$ it corresponds to strong concentration, and $n = 1$ relates to turbulent layer. For this reason, both f' and g increase with the increase in n.

The influences of second-order slip parameter, B, on f' and g are depicted in Figs. 13a–b. With the increase in B, f' increases and g decreases. However, the changes are very small. Indeed, Fig. 13a, b shows the negligible effects for $B = 0.0$, 0.5, and 1.0. But, for $B = 2.0$, f' and g show a considerable increment or decrement effect, respectively.

The impacts of first-order slip parameter, A, on f', g, and θ are described in Fig. 14a–c. It is seen that A has strong influence on f' and g. For larger A, f' increases but g decreases. A big change in f' and g is observed for changing A from 0.0 to
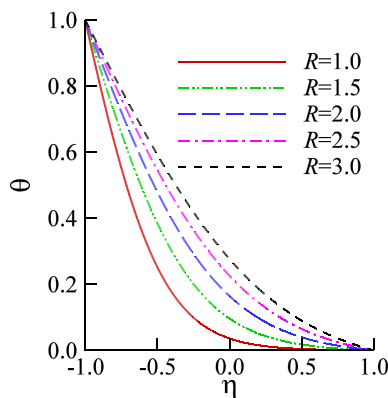

Fig. 17 Variations θ for higher R, when $\varphi = 0.05$, $M = 0.5$, $n = 0.5$, $K = 2.0$, $B = 1.0$, $A = 1.0$, and $S = 2.0$, and $\lambda = -1.0$

1.0. So, there is a big impact of the first-order slip parameter on f' and g.

Figure 15a–c shows the effects of magnetic field parameter, M, on f', g, and θ. Generally, the magnetic field controls the fluid flow. Here, the flow is considered through a channel. Figure 15a clears the increment of f' for higher M. Contrary to this, g shows a decreasing nature with higher M. However, θ exhibits negligible effect for larger M. With higher M, thermal does not show any significant effect on boundary increases.

The impacts of suction parameter, S, on f', g, and θ are elucidated in Fig. 16a–c. Results indicate that f' and θ decrease, but g significantly increases with larger S. The nonlinear decreasing pattern is recognized in f' due to the improvement in S. On the other hand, g attains its largest value for $S = 4.0$. For $S = 2.0$, 2.5, and 3.0, the decreasing rate is higher in θ compared to $S = 3.5$ and 4.0. The thermal boundary layer gradually decreases for larger S.

Figure 17 exhibits the influences of radiation parameter, R, only on θ. It is found that θ increases for larger R. The curve also shows that thermal boundary layer accelerates due to the augmenting in R. The reason for such behaviors is that

the higher radiation parameter leads to more heat owing to the collision of fluid particles.

4 Conclusion

In this study, the micropolar nanofluid flow in a shrinking channel has been investigated with the influence of second-order velocity slip, magnetic field and thermal radiation. Using the similarity variables, the governing equations are transformed into a system of ordinary differential equations. These are solved by the finite difference method. From the results, the following conclusions are drawn:

(i) Boundary layer separation is accelerated for higher suction parameter, second-order slip parameter and volume fraction of alumina nanoparticles, however, it is slowed down for increasing material constant, micro-rotation parameter, first-order slip parameter, and magnetic parameter.

(ii) Higher suction parameter leads to a decrease in skin friction coefficient and an increase in local Nusselt number.

(iii) Both skin friction coefficient and local Nusselt number are found to increase with the increase in micro-rotation parameter, material constant, first-order slip parameter, and magnetic parameter.

(iv) With the increase in material constant, first and second-order slip parameters, and magnetic parameter, the fluid velocity is increased, but the microrotation field is decreased.

(v) For increasing suction parameter, the temperature and the velocity of the fluid are decreased, whereas the microrotation field is increased.

The limitations of the current study are that the model is suitable for thermal equilibrium between the base fluid and nanoparticles and constant thermo-physical properties of the nanofluid. In this regard, the present model can be extended for non-equilibrium and temperature dependent thermo-physical cases.

Data availability The data that support the findings of this study are available from the corresponding author upon reasonable request.

Declarations

Conflict of interest The authors announce that they have no known competing financial interests or personal relationships that could have appeared to influence the work reported in this paper.

References

1. Saraswathy, M.; Prakash, D.; Muthtamilselvan, M.; Mdallal, Q.M.A.: Arrhenius energy on asymmetric flow and heat transfer of micropolar fluids with variable properties: a sensitivity approach. Alex. Eng. J. **61**, 12329–12352 (2022). https://doi.org/10.1016/j.aej.2022.06.015

2. Pasha, P.; Mirzaei, S.; Zarinfar, M.: Application of numerical methods in micropolar fluid flow and heat transfer in permeable plates. Alex. Eng. J. **61**, 2663–2672 (2022). https://doi.org/10.1016/j.aej.2021.08.040

3. Ur Rehman, K.; Khan, A.U.; Abbas, S.; Shatanawi, W.: Thermal analysis of micropolar nanofluid in partially heated rectangular enclosure rooted with wavy heated rods. Case Stud. Therm. Eng. **42**, 102701 (2023). https://doi.org/10.1016/j.csite.2023.102701

4. Mahmood, W.; Sajid, M.; Ali, N.; Sadiq, M.N.: A new interfacial condition for the peristaltic flow of a micropolar fluid. Ain Shams Eng. J. **13**, 101744 (2022). https://doi.org/10.1016/j.asej.2022.101744

5. Reddy, S.R.R.; Reddy, P.B.A.: Thermal radiation effect on unsteady threedimensional MHD flow of micropolar fluid over a horizontal surface of a parabola of revolution. Propuls. Power Res. **11**, 129–142 (2022). https://doi.org/10.1016/j.jppr.2022.01.001

6. Xiu, W.; Salawu, S.O.; Oludoun, O.Y.; Ogunlaran, O.M.; Disu, A.B.: Combined impact of Lorentz force, micro-rotation, and thermo-migration of particles: dynamics of micropolar fluids experiencing nonlinear thermal radiation and activation energy. J. Magnet. Magnet. Mater. **569**, 170447 (2023). https://doi.org/10.1016/j.jmmm.2023.170447

7. Patel, H.R.; Patel, S.D.; Darji, R.: Mathematical Study of unsteady micropolar fluid flow due to non-linear stretched sheet in the presence of magnetic field. Int. J. Therm. **16**, 100232 (2022). https://doi.org/10.1016/j.ijft.2022.100232

8. Sharma, R.P.; Mishra, S.R.: A numerical simulation for the control of radiative heat energy and thermophoretic effects on MHD micropolar fluid with heat source. J. Ocean Eng. Sci. **7**, 92–98 (2022). https://doi.org/10.1016/j.joes.2021.07.003

9. Singh, K.; Pandey, A.K.; Kumara, M.: Numerical solution of micropolar fluid flow via stretchable surface with chemical reaction and melting heat transfer using Keller–Box method. Propul. Power Res. **10**, 194–207 (2021). https://doi.org/10.1016/j.jppr.2020.11.006

10. Rehman, S.U.; Mariam, A.; Ullah, A.; Asjad, M.I.; Bajuri, M.Y.; Pansera, B.A.; Ahmadian, A.: Numerical computation of buoyancy and radiation effects on MHD micropolar nanofluid flow over a stretching/shrinking sheet with heat source. Case Stud. Therm. Eng. **25**, 100867 (2021). https://doi.org/10.1016/j.csite.2021.100867

11. Du, J.; Su, Q.; Li, L.; Wang, R.; Zhu, Z.: Evaluation of the influence of aggregation morphology on thermal conductivity of nanofluid by a new MPCD-MD hybrid method. Int. Commun. Heat Mass Transf. **127**, 105501 (2021). https://doi.org/10.1016/j.icheatmasstransfer.2021.105501

12. Jin, X.; Guan, H.; Wang, R.; Huang, L.; Shao, C.: The most crucial factor on the thermal conductivity of metal-water nanofluids: match degree of the phonon density of state. Powder Technol. **412**, 117969 (2022). https://doi.org/10.1016/j.powtec.2022.117969

13. Wang, R.; Feng, C.; Zhang, Z.; Shao, C.; Du, J.: What quantity of charge on the nanoparticle can result in a hybrid morphology of the nanofluid and a higher thermal conductivity? Powder Technol. **422**, 118443 (2023). https://doi.org/10.1016/j.powtec.2023.118443

14. Ali, L.; Ali, B.; Mousa, A.A.A.; Hammouch, Z.; Hussain, S.; Siddique, I.; Huang, Y.: Insight into significance of thermal stratification and radiation on dynamics of micropolar water based TiO_2 nanoparticle via finite element simulation. J. Mater. Res. Technol. **19**, 4209–4219 (2022). https://doi.org/10.1016/j.jmrt.2022.06.043

15. Esfahani, I.C.: A data-driven physics-informed neural network for predicting the viscosity of nanofluids. AIP Adv. **13**, 025206 (2023). https://doi.org/10.1063/5.0132846

16. Qasemian, A.; Moradi, F.; Karamati, A.; Keshavarz, A.; Shakeri, A.: Hydraulic and thermal analysis of automatic transmission fluid in the presence of nano-particles and twisted tape: an experimental and numerical study. J. Cent. South Univ. **28**, 3404–3417 (2021). https://doi.org/10.1007/s11771-021-4864-x

17. Sun, W.; Liu, Q.; Zao, J.; Ali, H.M.; Said, Z.; Liu, C.: Experimental study on sodium acetate trihydrate/glycerol deep eutectic solvent nanofluids for thermal energy storage. J. Mol. Liq. **372**, 121164 (2023). https://doi.org/10.1016/j.molliq.2022.121164

18. Liu, L.; Stetsyuk, V.; Kubiak, K.J.; Yap, Y.F.; Goharzadeh, A.; Chai, J.C.: Nanoparticles for convective heat transfer enhancement: heat transfer coefficient and the effects of particle size and zeta potential. Chem. Eng. Commun. **206**, 761–771 (2019). https://doi.org/10.1080/00986445.2018.1525364

19. Bazmi, M.; Askari, S.; Ghasemy, E.; Rashidi, A.; Ettefaghi, E.: Nitrogen-doped carbon nanotubes for heat transfer applications: enhancement of conduction and convection properties of water/N-CNT nanofluid. J. Therm. Anal. Calori. **138**, 69–79 (2019). https://doi.org/10.1007/s10973-019-08024-y

20. Wang, R.; Chen, T.; Qi, J.; Du, J.; Pan, G.; Huang, L.: Investigation on the heat transfer enhancement by nanofluid under electric field considering electrophorestic and thermophoretic effect. Case Stud. Therm. Eng. **28**, 101498 (2021). https://doi.org/10.1016/j.csite.2021.101498

21. Ahmed, N.; Tassaddiq, A.; Alabdan, R.; Adnan, U.; Khan, S.; Noor, S.; Mohyud-Din, S.T.; Khan, I.: Applications of nanofluids for the thermal enhancement in radiative and dissipative flow over a wedge. Appl. Sci. **9**, 1976 (2019). https://doi.org/10.3390/app9101976

22. Salahuddin, T.; Khan, M.; Al-Mubaddel, F.S.; Alam, M.M.; Ahmad, I.: A study of heat and mass transfer micropolar fluid flow near the stagnation regions of an object. Case Stud. Therm. Eng. **26**, 101064 (2021). https://doi.org/10.1016/j.csite.2021.101064

23. Abbas, N.; Saleem, S.; Nadeem, S.; Alderremy, A.A.; Khana, A.U.: On stagnation point flow of a micro polar nanofluid past a circular cylinder with velocity and thermal slip. Res. Phys. **9**, 1224–1232 (2018). https://doi.org/10.1016/j.rinp.2018.04.017

24. Ali, B.; Shafiq, A.; Siddique, I.; Al-Mdallal, Q.; Jarad, F.: Significance of suction/injection, gravity modulation, thermal radiation, and magnetohydrodynamic on dynamics of micropolar fluid subject to an inclined sheet via finite element approach. Case Stud. Therm. Eng. **28**, 101537 (2021). https://doi.org/10.1016/j.csite.2021.101537

25. Wang, G.; Zhang, Z.; Wang, R.; Zhu, Z.: A review on heat transfer of nanofluids by applied electric field or magnetic field. Nanomaterials **10**, 2386 (2020). https://doi.org/10.3390/nano10122386

26. Goud, B.S.; Nandeppanavar, M.M.: Ohmic heating and chemical reaction effect on MHD flow of micropolar fluid past a stretching surface. Part. Diff. Eq. Appl. Math. **4**, 100104 (2021). https://doi.org/10.1016/j.padiff.2021.100104

27. Yadav, P.K.; Kumar, A.: An inclined magnetic field effect on entropy production of non-miscible Newtonian and micropolar fluid in a rectangular conduit. Int. Commun. Heat Mass Transf. **124**, 105266 (2021). https://doi.org/10.1016/j.icheatmasstransfer.2021.105266

28. Yusuf, T.A.; Kumar, R.N.; Prasannakumara, B.C.; Adesanya, S.O.: Irreversibility analysis in micropolar fluid film along an incline porous substrate with slip effects. Int. Commun. Heat Mass Transf. **126**, 105357 (2021). https://doi.org/10.1016/j.icheatmasstransfer.2021.105357

29. Usafzai, W.K.; Aly, E.H.: Multiple exact solutions for micropolar slip flow and heat transfer of a bidirectional moving plate. Therm. Sci. Eng. Prog. **37**, 101584 (2023). https://doi.org/10.1016/j.tsep.2022.101584

30. Kumar, K.A.; Sugunamma, V.; Sandeep, N.; Mustafa, M.T.: Simultaneous solutions for frst order and second order slips on micropolar fuid fow across a convective surface in the presence of Lorentz force and variable heat source/sink. Sci. Rep. **9**, 14706 (2019). https://doi.org/10.1038/s41598-019-51242-5

31. Su, J.: Suitable weak solutions to the micropolar fluids model in a bounded domain. J. Math. Anal. Appl. **504**, 125406 (2021). https://doi.org/10.1016/j.jmaa.2021.125406

32. Slayi, S.; Arwadi, T.E.; Dib, S.: Stabilized Gauge Uzawa scheme for an incompressible micropolar fluid flow. Appl. Numer. Math. **167**, 45–72 (2021). https://doi.org/10.1016/j.apnum.2021.04.003

33. Sherief, H.H.; Faltas, M.S.; Ragab, K.E.: Motion of a slip spherical particle near a planar micropolar-viscous interface. Eur. J. Mech. B Fluids **89**, 274–288 (2021). https://doi.org/10.1016/j.euromechflu.2021.06.004

34. Habib, U.; Abdal, S.; Siddique, I.; Ali, R.: A comparative study on micropolar, Williamson, Maxwell nanofluids flow due to a stretching surface in the presence of bioconvection, double diffusion and activation energy. Int. Commun. Heat Mass Transf. **127**, 105551 (2021). https://doi.org/10.1016/j.icheatmasstransfer.2021.105551

35. Rees, D.A.S.; Pop, I.: Free convection boundary-layer flow of a micropolar fluid from a vertical flat plate. IMA J. Appl. Math. **61**, 179–197 (1998). https://doi.org/10.1093/imamat/61.2.179

36. Cortell, R.: Effects of viscous dissipation and radiation on the thermal boundary layer over a nonlinearly stretching sheet. Phys. Lett. A **372**, 631–636 (2008). https://doi.org/10.1016/j.physleta.2007.08.005

37. Nayak, M.K.; Hakeem, A.K.; Abdul, A.K.; Makinde, O.D.: Time varying chemically reactive magneto-hydrodynamic non-linear falkner-skan flow over a permeable stretching/shrinking wedge: Buongiorno model. Journal of Nanofluids **8**(3), 467–476 (2019)

38. Hashim, M.; Khan, A.S.: Alshomrani, Numerical simulation for flow and heat transfer to Carreau fluid with magnetic field effect: dual nature study. J. Magn. Magn. Mater. **443**, 13–21 (2017)

39. Rosseland, S.: Astrophysik: Auf Atomtheoretischer Grundlage. Springer, Berlin (1931)

40. Ishak, A.; Yacob, N.A.; Bachok, N.: Radiation effects on the thermal boundary layer flow over a moving plate with convective boundary condition. Meccanica **46**, 795–801 (2011). https://doi.org/10.1007/s11012-010-9338-4

41. Magyari, E.; Pantokratoras, A.: Note on the effect of thermal radiation in the linearized Rosseland approximation on the heat transfer characteristics of various boundary layer flows. Int. Commun. Heat Mass Transf. **38**, 554–556 (2011). https://doi.org/10.1016/j.icheatmasstransfer.2011.03.006

42. Blottner, F.G.: Finite difference methods of solution of the boundary-layer equations. AIAA J. **8**(2), 193–205 (1970). https://doi.org/10.2514/3.5642

43. Takhar, H.S.; Soundalgekar, V.M.: Flow and heat transfer of a micropolar fluid past a continuously moving porous plate. Int. J. Eng. Sci. **23**(2), 201–205 (1985). https://doi.org/10.1016/0020-7225(85)90074-6

44. Jena, S.K.; Mathur, M.N.: Free convection in the laminar boundary layer flow of a thermomicropolar fluid past a vertical flat plate with suction/injection. Acta Mech. **42**, 227–238 (1982). https://doi.org/10.1007/BF01177194